Activation of nickel foam through *in-liquid* plasma-induced phosphorus incorporation for efficient quasi-industrial water oxidation and selective oxygenation of organics

Hongyuan Yang [a,1], Pramod V. Menezes [b,1], Guoliang Dai [c], Gonela Vijaykumar [a], Ziliang Chen [a], Mohammad Al-Shakran [b], Timo Jacob [b,d,e], Matthias Driess [a], Prashanth W. Menezes [a,f,*]

[a] *Department of Chemistry: Metalorganics and Inorganic Materials, Technical University of Berlin, Straße des 17 Juni 135. Sekr. C2, 10623 Berlin, Germany*
[b] *Institute of Electrochemistry, Ulm University, Albert-Einstein-Allee 47, 89081 Ulm, Germany*
[c] *School of Chemistry and Life Sciences, Suzhou University of Science and Technology, Suzhou 215009, PR China*
[d] *Helmholtz-Institute Ulm (HIU) Electrochemical Energy Storage, Helmholtzstraße 11, 89081 Ulm, Germany*
[e] *Karlsruhe Institute of Technology (KIT), P.O. Box 3640, 76021 Karlsruhe, Germany*
[f] *Materials Chemistry Group for Thin Film Catalysis–CatLab, Helmholtz-Zentrum Berlin für Materialien und Energie, Albert-Einstein-Str. 15, 12489 Berlin, Germany*

ARTICLE INFO

ABSTRACT

Developing bifunctional electrodes for oxidation catalysis is highly desirable for hydrogen and value-added chemicals production. Herein, we directly activate the nickel foam through the incorporation of elemental P (P-NF) using a facile, controllable, and ultrafast *in-liquid* plasma electrolysis approach. When serving for oxygen evolution reaction (OER) in 1 M KOH at room temperature, the optimized P-NF can afford 500 mA cm^{-2} at 350 mV, and stabilize this current density for over 120 h. Remarkably, the electrode maintains a stable industrial-grade current density in an assembled electrolyzer under quasi-industrial conditions (60 ℃ and 6 M KOH) for over 107 h. The combination of *ex/in-situ* characterizations and theoretic calculations unequivocally illustrates that P-incorporation induces an elevated electrode porosity and wettability, increased and immobilized Fe impurity doping, as well as enhanced conductivity, forming active Fe-doped γ-Ni^{III}OOH during OER. The practical bifunctionality of P-NF is additionally verified with selective oxygenation of organics forming value-added chemicals.

1. Introduction

The gradually emerging green hydrogen (H$_2$) fuel with high energy density is regarded as an effective alternative to traditional fossil fuels [1–4]. Generating high-purity H$_2$ fuel by sustainable and environmental-friendly water electrolysis has gained global research interest, while its kinetically sluggish anodic oxygen evolution reaction (OER), involved in the complex four-electron/proton-coupled transfer, is considered as the bottleneck half reaction limiting the efficiency of water electrolysis [5–9]. In analogy to OER, the anodic selective electrooxidation of organic compounds also tends to be based on a multi-step electron transfer process, which can produce value-added chemical products with water as the oxygen source in a more efficient

and greener way [10,11]. Therefore, uncovering economically- and environmentally-friendly bifunctional anodic electrocatalysts that can catalyze the oxidation of water and organic substrates into oxygen and value-added chemicals, respectively, is of the highest importance both for fundamental research and industrial applications [12–14].

Currently, the most practically commercialized water electrolysis devices are the alkaline water electrolyzers (AWEs), in which the anodes are usually made of low-cost Ni and its alloys (*e.g.*, Raney nickel), exhibiting moderate working performance [15,16]. Despite extensive efforts devoted to designing emerging transition metal (TM)-based materials as both cheap and active catalysts (electrodes) for OER, the majority of them can only be effective under laboratory conditions rather than in more harsh industrial water electrolyzers (elevated temperature

of 60 °C and electrolyte concentration of 6 M KOH, as well as delivering a current density of 200–400 mA cm^{-2} [16,17]. Among them, owing to the three-dimensional macroporous feature, good mechanical strength, and superior electrical conductivity, nickel foam (NF) has been widely utilized as substrates integrated with the catalysts as electrodes in water electrolyzers [16,18,19]. More intriguingly, by using calcination, hydro (solvo)thermal synthesis, gas-phase plasma treatment, and ambient wet chemical methods, NF can also derive various Ni-based compound catalysts on its surface [20–24], functioning as excellent water splitting electrodes. In fact, Mullins et al. even found that bare NF with a hierarchically porous structure can directly serve as an OER electrode in unpurified 1 M KOH, which *in-situ* reconstructed into highly active $NiO_x(OH)_y$ through Fe-impurity doping from the electrolyte showing moderate activity [25]. Following a series of previously reported valuable works, it is worth mentioning that under alkaline OER conditions, the incorporation of more Fe-impurities ($\leq$ 10%) from KOH into the Ni film can facilitate the transformation into $Ni_{1-x}Fe_xOOH$ with higher activity [26–29]. However, owing to the detrimental working environment, highly oxidizing reaction conditions, inferior chemical robustness, as well as relatively poor intrinsic conductivity, such Ni-based compounds (deriving from the surface of NFs) have been rarely reported to show satisfactory OER performance at higher current densities and under (quasi-)industrial conditions [16,17].

Recently, heteroatomic P incorporation represents one of the most promising approaches to improving the activity and stability of TM catalysts for water electrolysis, which can effectively modulate the electronic structure, improve electronic conductivity, as well as enhance chemical stability and corrosion resistance of the catalysts [16,30–34]. Based on these points, the incorporation of P atoms into NF, *i.e.*, (near) surface metallic Ni layer, is expected to enable an exceptional catalytic ability for water oxidation, even under harsh industrial environments. Moreover, such modified NF might also be suitable for the efficient electrooxidation of organic substrates undergoing an anodic catalytic process similar to OER. To our knowledge, such activated heteroatom-incorporated NF electrodes have not been reported so far, probably due to the lack of an appropriate fabrication method because TM phosphides are more easily formed as unwanted by-products when incorporating P into unstable TM host lattice [33]. Considering that NF-derived Ni_xP_y phosphides were typically obtained by reacting the metallic Ni with PH_3 vapor *via* pyrolysis, in principle, lowering the amounts of phosphorus source (*e.g.*, sodium hypophosphite) could realize P-incorporation [20,32,35,36], yet such a long-term thermal treatment increases the complexity and contamination, not conducive to practical applications. In this context, the ultrafast in-liquid cathodic plasma electrolysis (CPE), in which the metallic substrates as cathodes are immersed into a certain electrolyte and processed by continuous sparking under a relatively high applied voltage, could provide an effective solution [37–39]. This is based on the fact that CPE can harden various metallic substrates by driving different elements into the surface metal lattices within a very short period of time (a few minutes) with increased surface roughness and porosity [37,38,40]. Nevertheless, so far CPE has not been adopted to drive P atom diffusion into metallic substrates, and hence such a versatile approach could be highly interesting to activate NF for practical water electrolysis.

In view of the above introduction, the following research questions arose, which have been addressed in this work: i) can one rapidly and controllably incorporate P atoms into the (near)surface of NF using the CPE method?; If so, ii) what is the effect of the P atom-incorporation strategy?; iii) Can the P-incorporated NF be used as electrodes for efficient OER?; If yes, iv) are such treated NF capable of robustly operating and remaining stable under (quasi-)industrial electrolysis conditions?; v) Will the OER-driven reconstructed surface-active structure of this CPE-treated NF be similar to that of bare NF?; vi) Can we extend this approach to anodic electrooxidation of organic substrates to obtain value-added products?

In response to these questions, for the first time, we employed the

CPE method to successfully activate the NF by incorporating P atoms into its (near)surface metallic Ni layer, where different CPE durations can linearly modify the extent of P incorporation within merely a few minutes. Compared with the untreated NF, the treated P-NF exhibited distinctly elevated electrical conductivity, improved surface porosity and wettability, and better adsorption ability of impurity Fe ions from KOH electrolyte. Thus, the P-NF prepared at an optimized CPE time (10 min) can drive and maintain 500 mA cm^{-2} at only ~350 mV overpotentials for over 120 h under **ambient laboratory** conditions (**room temperature and 1 M KOH**). In particular, when serving as an anode for a **quasi-industrial** water electrolyzer (**60 °C and 6 M KOH**), it can reach the same current density at a cell voltage of only ~1.72 V (far beyond the current industrial criterion) [17], and further maintains this industrial-grade current density up to 107 h. By using a combination of *ex/in-situ* characterizations we could reveal that during the OER process, the anodic oxidation and leaching of P resulted in an increased surface porosity of P-NF, which contributed to stabilizing Fe dopants at the surface, thus achieving a complete surface reconstruction into highly active Fe^{III}-doped γ-$Ni^{III}OOH$. Conversely, bare NF with a relatively more smooth surface cannot immobilize any Fe dopant at the electrode surface during OER, where only pure γ-$Ni^{III}OOH$ was formed, while the doped Fe atoms merely existed in the near-surface region of the bare NF electrode, hardly participating in catalysis process. This accounted for a much higher catalytic performance of CPE-treated P-NF during long-term water oxidation. In addition, we demonstrate that the P-NF-based anode can be employed to oxidize furan-2-carboxaldehyde and acetaldehyde (CH_3CHO) into furan-2-carboxylic acid and acetic acid, respectively, with high efficiency and selectivity, verifying its superior bifunctional oxidation activity.

2. Experimental section

2.1. Chemicals and materials

Deionized water was used to carry out all the experiments. Commercially available potassium hydroxide (1 M KOH, Fe was ~0.05 ppm determined by ICP-AES), ethanol, hydrochloric acid (HCl, 30%, suprapure), and 5 wt% Nafion were obtained from Sigma Aldrich. Selected iridium oxide (IrO_2), platinum (20%) on carbon black (20% Pt/C), and sodium hypophosphite (NaH_2PO_2 H_2O) were purchased from Alfa Aesar. The electrode substrates nickel foam (NF) was obtained from Recemat BV.

2.2. Preparation of P-NF with different catholic plasma electrolysis (CPE) time

The CPE method was employed in the present work for P-incorporation into bare NF, and the optical image of such a plasma electrolysis setup can be found in Fig. S1. Also, a detailed introduction to the approach has been elaborated in the section "*Supplementary details of the cathodic plasma electrolysis (CPE) method*" and Fig. S2 in Supporting Information. Briefly, P-NF was fabricated in a double-walled glass cell containing 200 mL of 0.01 M NaH_2PO_2, where stainless steel plate (dimension: 20 mm x 20 mm x 2 mm) was used as a counter electrode and Ni foam (diameter: 8 mm) as a working electrode. Before the measurement, NF was ultrasonically cleaned in 1 M HCl and ethanol for 10 min, respectively, and then rinsed with deionized water and dried in a stream of warm air. A water-cooling system was used to control the temperature of the electrolyte between 30 and 50 °C. A maximum voltage (630 V) from the DC power supply (TDK-Lambda programable, GEN600–1.3/E, 1 U, 780 W, RS-232/RS-485) was applied to synthesize the catalyst. After the experiment, the prepared electrodes were thoroughly rinsed with deionized water and dried in an N_2 gas flow. The NF was treated by CPE for 1, 5, 10, and 15 min and was denoted as P-NF-1, P-NF-5, P-NF-10, and P-NF-15, respectively, in the current work. Note that these P-NF electrodes were fabricated by diffusing P atoms into the

near-surface region of bare NF substrates, where their mass barely changed after P incorporation.

2.3. Preparation of NiPt₃ @NiS, Pt/C, and IrO₂ on NF

The preparation detail of NF-supporting $NiPt_3$@NiS, Pt/C, and IrO_2 is provided in the Supporting Information.

2.4. Characterization

Powder X-ray diffraction (PXRD), scanning electron microscopy (SEM) with energy-dispersive X-ray (EDX) mapping (also coupled with a focused ion beam, FIB), transmission electron microscopy (TEM), contact angle (CA), X-ray photoelectron spectroscopy (XPS), and quasi-*in-situ* Raman characterizations were employed in the current work and their details have been elaborated in Supporting Information.

2.5. Electrochemical measurements

Electrochemical measurements were carried out in a standard three or two-electrode system in laboratory conditions (1 M KOH and room temperature) and industrial conditions (6 M KOH and 60 ℃) controlled by a potentiostat (SP-200, BioLogic Science Instruments) equipped with the EC-Lab v10.20 software package. The synthesized samples were utilized as the working electrodes, while Pt wire (0.5 mm diameter × 230 mm length; A-002234, BioLogic) and Hg/HgO (CH Instruments, Inc.) served as the counter electrode and reference electrode, respectively. Cyclic voltammetry (CV), linear sweep voltammetry (LSV), and chronopotentiometry (CP) experiments were carried out with an applied *iR* compensation of 85%. The CV and LSV tests were performed at a scan rate of 5 mV s⁻¹. All measured OER potentials in laboratory conditions were calibrated with respect to a reversible hydrogen electrode (RHE) based on the following equation: E(RHE) = E(Hg/HgO) + 0.098 V + (0.059 × pH) V. When assembling two-electrode cells for overall water splitting test, the as-reported $NiPt_3$@NiS on NF was employed as the cathode.

Tafel slopes were determined by steady-state measurements through chronoamperometry (CA) with a stable potential of 5 min from an interval of 15 mV. The average current values obtained at each potential were used for the calculation of Tafel plots. To assess the electrochemical double-layer capacitance (C_{dl}), CV was performed at a non-Faradaic voltage region. Given that C_{dl} is linearly proportional to electrochemically active surface area (ECSA), we have normalized the current values to their C_{dl} [12]. The electrochemical impedance spectroscopy (EIS) was recorded at 1.52 V (*vs.* RHE) to attain the Nyquist plots. The amplitude of the sinusoidal wave was determined in a frequency range of 100 kHz to 1 mHz. The Faradic efficiency (FE) was calculated by comparing the amount of experimentally produced O_2 and that of theoretically calculated gas according to the Faradic equation: FE= (4 *V*F) / (V_m*Q). V, F, V_m, and Q represent the volume of experimentally evolved O_2 (mL), Faraday constant (96485 C mol⁻¹), molar volume (24.5 L mol⁻¹, RT), and the total amount of electrical charge (C), respectively. The amount of evolved gas was measured by the drainage method at a constant current of 50 mA for 3600 s [6]. The turnover frequency (TOF) was calculated through the equation, TOF (s⁻¹) = (j × N_A) / (z × F × n), where z = 4 for OER, while j, N_A, F, and n represent the current density (A cm⁻²), Avogadro number (6.02 ×10²³), Faraday constant (96485 C mol⁻¹), and the number of electrochemically redox active sites (Ni) participating in the OER process, respectively [12].

2.6. Bulk electrolysis of organic substrates and product analysis

Bulk electrolysis was performed under constant potential (1.49 V *vs.* RHE) in a three-electrode cell set-up the same as OER tests, where 10 mL of 1 M KOH was used as the electrolyte with the addition of 0.1 M

desired organic substrates. The reactivity and the corresponding organic product formation during the electrooxidation reaction of different substrates were analyzed by ¹H nuclear magnetic resonance (¹H NMR) spectroscopy in a 400 MHz JEOL NMR instrument and quantified with dimethyl sulfone (0.166 mmol) as an internal standard. All the spectra were analyzed in MestReNova software. Each spectrum consisted of a sharp peak at 4.7 ppm associated with residual H_2O (aqueous solution of 1 M KOH) and chemical shift values of the protons of the organic compounds were assigned accordingly and compared with literature values of the known compounds. The organic compounds are quantified (chemical conversion) by calculating the relative intensity of the proton signals. Chemical conversion and FE were calculated following equations:

Chemical conversion (%) = [n (product) / n (internal standard)] · 100%;.

FE (%) = [n (product formed) · n_e · F / (Q)] · 100%, where F, n, n_e, and Q represent the Faraday constant (96 485 C mol⁻¹), the mol of product quantified from ¹H NMR, the electrons needed for the oxidation process, and the charge (coulombs) passed through the solution.

2.7. Theoretical calculations

Density functional theory (DFT) calculations were utilized to elucidate the total density of state (TDOS) and adsorption energy towards Fe (ΔE_{Fe}). The associated details can be seen in Supporting Information.

3. Results and discussion

3.1. Characterizations of as-prepared P-NF electrodes

Fig. 1a illustrates the synthesis of the P-NF electrode through CPE, where bare NF and stainless steel were employed as cathode and anode, respectively, in an 0.01 M NaH_2PO_2·H_2O electrolyte. Under the applied cathodic potential, the plasma was continuously glow discharged at the surface of the NF electrode within a short period of time (1, 5, 10, and 15 min, denoted as P-NF-1, P-NF-5, P-NF-10, and P-NF-15), converting the hypophosphite anions into elemental phosphorus, and diffusing them into the surface metallic Ni lattices. As a consequence, the as-treated NF turned black, indicating the formation of P-incorporated NF (optical image and the associated crystalline structures are shown in Fig. 1b). At the same time, DFT calculations reveal the incorporated P atoms tend to partially substitute the Ni atoms rather than penetrate into the lattice interstitials of the metallic Ni matrix (Fig. 1b and Fig. S3). The successful incorporation of P atoms into bare NF surface has been confirmed with a series of experimental characterizations, including (FIB-)SEM with EDX mapping, PXRD, as well as surface and depth profiling XPS. As the activity of P-NF was found to be maximum after 10 mins of CPE treatment (see OER activity section), the details of characterization have been only discussed for P-NF-10. The as-obtained SEM-EDX findings for P-NF-10 disclose that 7% P atoms (from surface EDX) were homogeneously introduced into the NF with a depth of around 1.5 µm (Fig. 1c–e, Figs. S4−S6, and Tables S1−S2). It is worth noting that P-NF-10 samples fabricated at different batches exhibit almost identical SEM together with the associated EDX results, corroborating the high reproducibility of our CPE method (Figs. S7−S8, and Table S3). In addition, from the PXRD pattern of P-NF-10, no new peaks were observed except the diffraction peaks of the corresponding NF (PDF#04−0850), illustrating that the introduction of P atoms did not distinctly modify the crystalline structure of the host NF material, in agreement with the previous reports [32]. Nevertheless, the careful examination revealed that in comparison with that of bare NF, the diffraction peaks assigned to the (111) facet of the Ni phase of P-NF-10 slightly positive shifted (Fig. 1 f). This is consistent with the results of the aforementioned DFT calculations and related previous reports, that is, P atoms with a smaller atomic radius partially substituted the relatively larger Ni atoms, leading to a lattice contraction [30,33]. This can be
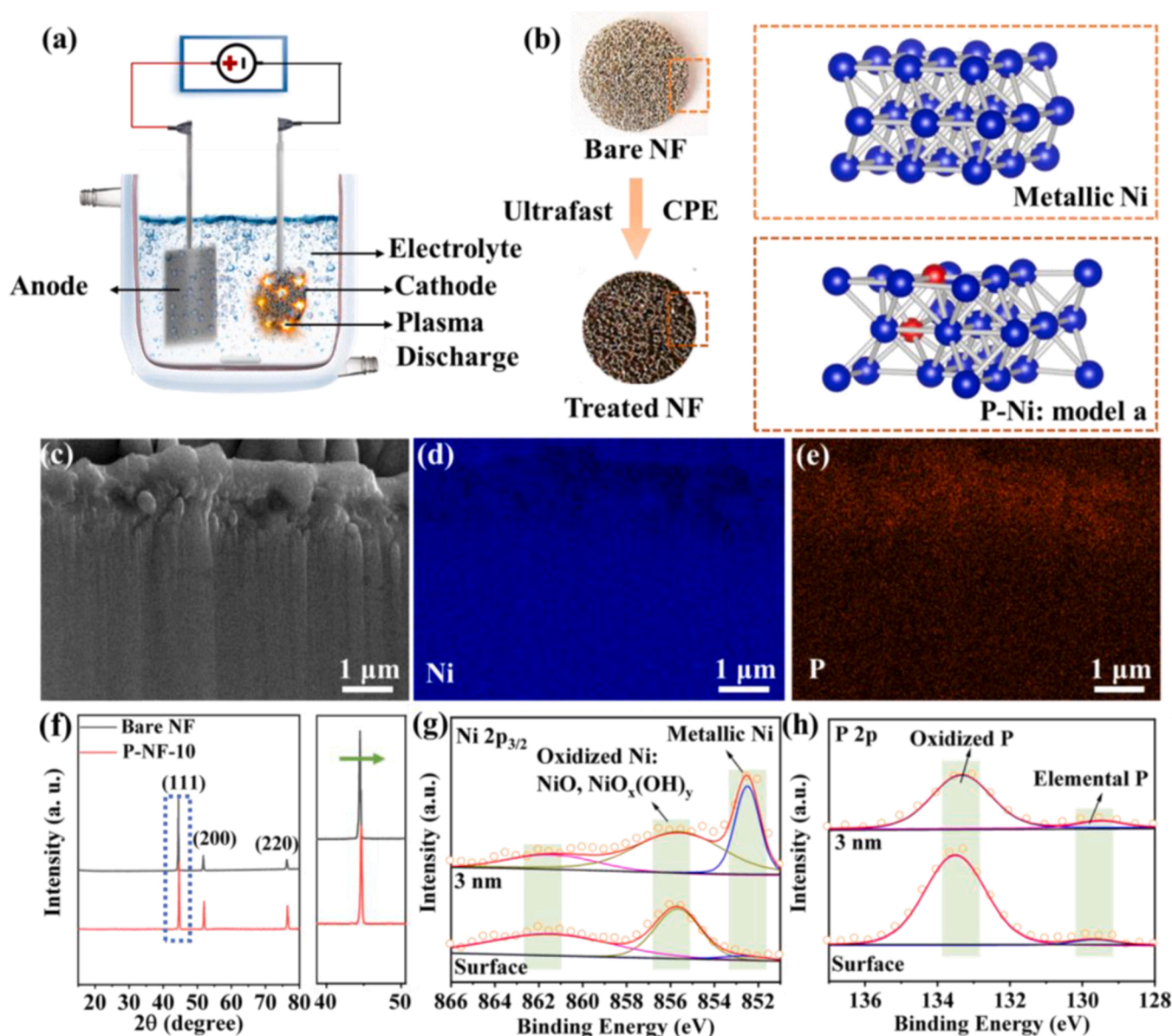
Fig. 1. (a) The schematic illustration of the CPE treatment for bare NF; (b) Optical images of bare NF and P-NF treated by CPE, as well as their corresponding surface crystalline structure, *i.e.*, pure metallic Ni, as well as P incorporated metallic Ni (the **model a** of P-Ni, and the other models of P-NF are shown in Fig. S3). Note that the blue and red spheres represent Ni and P atoms, respectively; (c) Cross-sectional FIB-SEM image of P-NF-10 with the associated EDX elemental mapping of (d) Ni, and (e) P. (f) PXRD patterns of P-NF-10 and bare NF with the magnification of the diffraction peaks assigned to Ni (111) facet; Surface and depth profiling (at ~3 nm) XPS spectra of (g) Ni $2p_{3/2}$, and (h) P 2p for P-NF-10.

further verified by identifying the lattice fringe of P-NF-10 (0.174 nm, assigned to (200) crystal facet of metallic Ni) *via* high-resolution (HR) TEM characterization that was a little smaller than the theoretic value (0.176 nm, PDF#04–0850) (Fig. S9). Besides, the successful P-incorporation can also be corroborated by comparing the high-resolution Ni surface XPS spectra for bare NF and P-NF-10 (Fig. S10). Note that although P-Ni was partially oxidized due to air and electrolyte exposure (forming NiO_xH_y species and PO_x), the depth profiling elaborates that the deeper the electrode region, the more incorporated elemental P with the less oxidized species (Fig. 1 g–h) [25,41].

Since the incorporation of P into NF triggered the formation of a porous surface (Fig. 2a–b and Figs. S11–S12), the corresponding surface wettability and electronic structure were further investigated. P-NF-10 displayed superhydrophilicity with a CA of 0°, while the untreated bare NF had a hydrophobic surface (CA = 121.8°) (insets of Fig. 2a–b). Consequently, the contact and penetration of electrolyte towards P-NF

were tremendously elevated, which can facilitate the utilization of active sites of P-NF [20,25]. Accordingly, more access was offered to Fe impurities from the electrolyte to diffuse into the P-NF surface during OER. Indeed, the presence of incorporated P can also promote and facilitate the uptake of impurity Fe in the electrolyte, which is substantiated by our theoretical calculations on the adsorption ability towards Fe atoms of the above-established P-incorporated metallic Ni and pure metallic Ni models. P-Ni with various P-incorporating states show significantly optimized ΔE_{Fe} than pure Ni metal, confirming their improved surface adsorption capability towards Fe atoms (Fig. S13 and Fig. 2c). As a result, in the utilized unpurified 1 M KOH media, the redox peaks in the cyclic voltammetry (CV) curve of P-NF-10 shifted positively compared with those of bare NF, which can usually be observed for Ni film catalysts in electrolytes with higher Fe contents (Fig. S14) [25,28, 29]. Additionally, as reflected by the calculations of TDOS, P-NF exhibited a significantly increased electron number around the Fermi
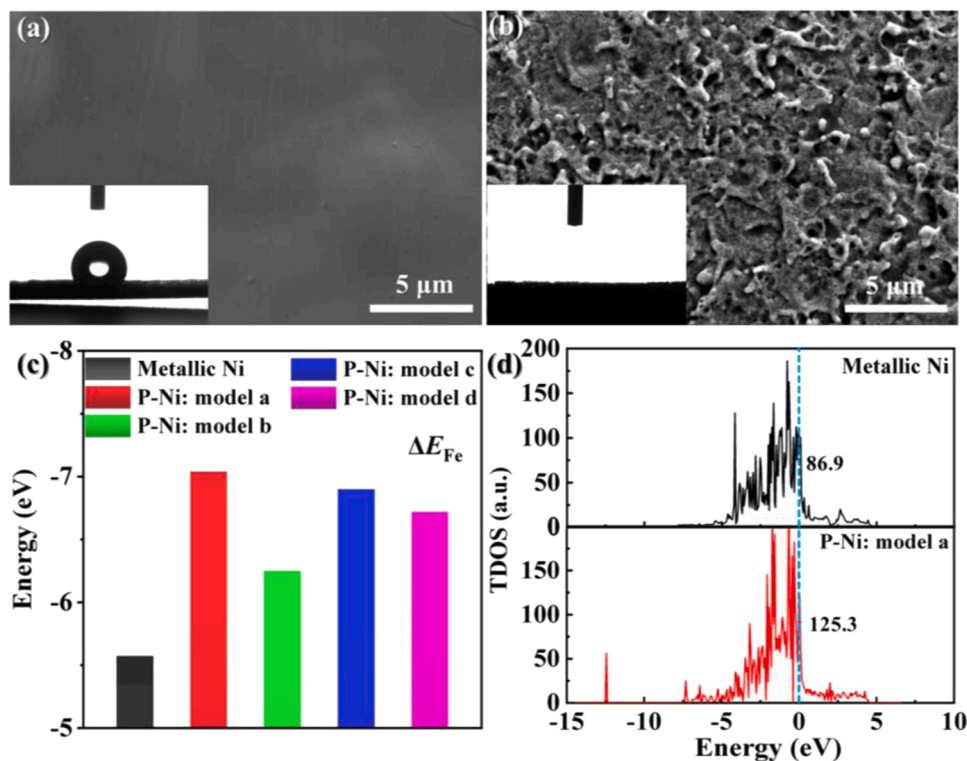
Fig. 2. The SEM images of (a) bare NF with a flat and smooth surface, and (b) P-NF-10 with a significantly porous and rough surface. The insets in Fig. 2a and b are the CA of bare NF and P-NF-10, respectively; (c) The ΔE_{Fe} of metallic Ni and various P-Ni models with different P-incorporation states; (d) The calculated TDOS of pure metallic Ni model (bare NF), and P incorporated metallic Ni (**model a** of P-Ni was adopted here, and the TDOS of other P-Ni models were displayed in Fig. S15).
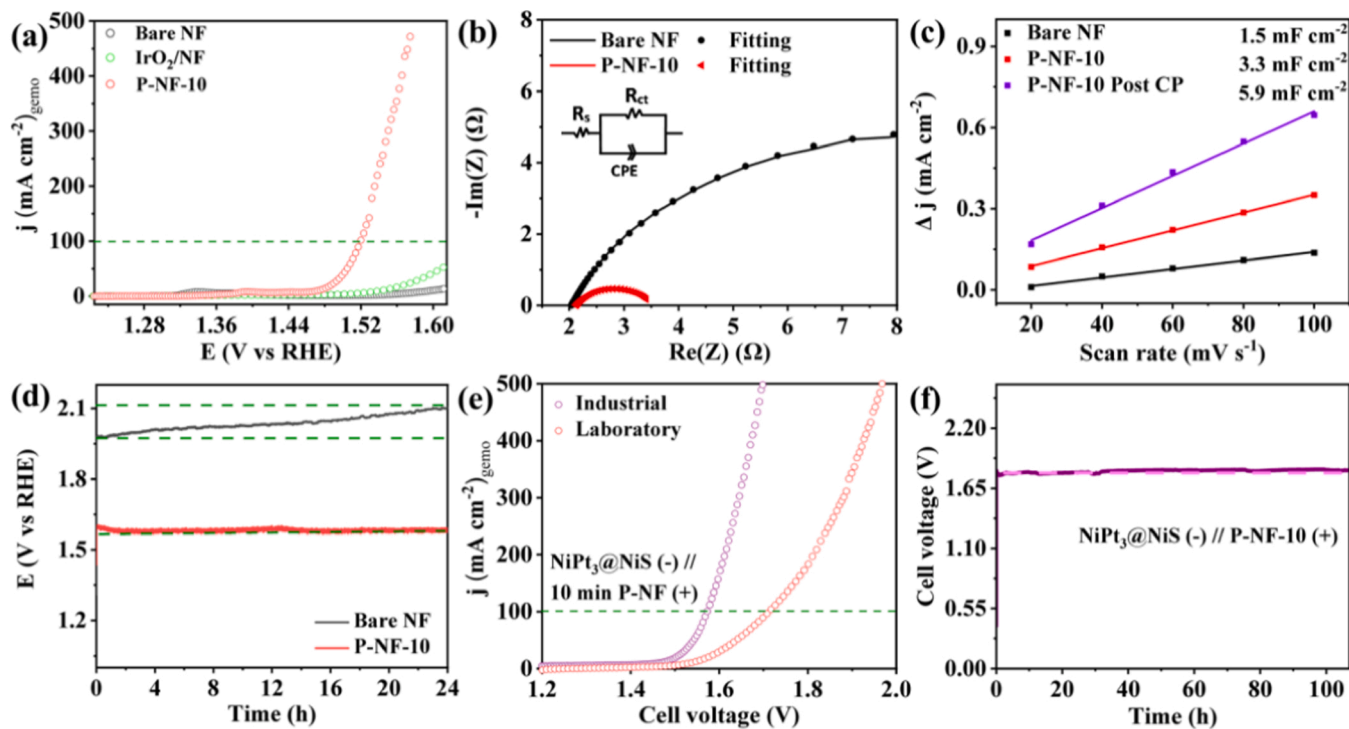

Fig. 3. (a) The OER LSV curves normalized against the geometric area of P-NF-10, IrO_2/NF, and bare NF at a scan rate of 5 mV s^{-1} in 1 M KOH under room temperature; (b) Nyquist plot of P-NF-10 and bare NF obtained from EIS fitting to equivalent circuits (inset) at an anodic potential of 1.52 V (*vs.* RHE); (c) C_{dl} values of bare NF, as well as P-NF-10 before and after laboratory-level CP calculated from their associated CV curves at non-Faradic region; (d) 24 h CP of P-NF-10 and bare NF at 500 mA cm^{-2} in 1 M KOH under room temperature; (e) LSV curves of $NiPt_3$@NiS (-) // P-NF-10 (+) normalized against the geometric area of P-NF-10 at a scan rate of 5 mV s^{-1} under laboratory and industrial conditions; (f) Over 107 h CP of $NiPt_3$ @NiS (-) // P-NF-10 (+) at 500 mA cm^{-2} under industrial conditions measured with a stirring speed of 1000 rpm.

level compared to pure metallic Ni, suggesting that the activated P-Ni layer had a strong positive effect on conductivity (Fig. 2d and Fig. S15) [20].

3.2. Electrocatalytic OER performance

The electrochemical OER performance of CPE-induced P-NF-10, as well as with the reference samples, including noble metal IrO$_2$ deposited on NF (IrO$_2$/NF), and a bare NF electrode (metallic Ni is usually applied as electrodes in the industrial AWEs), were also evaluated under laboratory conditions (1 M KOH and room temperature) *via* a standard three-electrode cell [42]. The LSV curves of P-NF-10 delivered 100 and 500 mA cm^{-2} current density at an ultralow overpotential of only ~297 and ~350 mV, respectively, which was much superior to the IrO$_2$/NF and bare NF (Fig. 3a). The obtained catalytic activity also outperformed the majority of the previously reported NF and other metal foam-derived electrodes for alkaline OER (Table S4). Simultaneously, the excellent electrocatalytic kinetics of P-NF-10 could be verified by its small Tafel slope value of 40.9 mV·dec^{-1} (Fig. S16), comparable to most reported efficient NiFe benchmark catalysts [27,28]. The fitted Nyquist plots together with the equivalent circuit scheme obtained from the EIS measurements (Fig. 3b and Table S5) suggest that P-NF-10 had a superior rapid charge-transfer ability, whose charge transfer resistance (R_{ct}, 1.391 Ω) was significantly lower than that of bare NF (13.38 Ω). On the other hand, the ECSA which directly reflects the number of active sites between P-NF and bare NF was also assessed through C_{dl} determination. Fig. 3c and Fig. S17 show P-NF-10 presented the highest C_{dl} of 3.3 mF cm^{-2}, 2.2 times the value of bare NF (1.5 mF cm^{-2}), indicating more exposed active surface after incorporating P into NF. As the C_{dl} value is proportional to the ECSA, the LSV curves normalized to the C_{dl} further revealed that P-NF endowed a distinctly higher intrinsic OER activity (Fig. S18). The boost in inherent activity induced by P-incorporating can be further verified by the excellent TOF of P-NF-10 which was substantially higher than that of bare NF (Fig. S19). Similarly, to affirm the sustained stability of P-NF-10, CP measurements were carried out at a high current density of 500 mA cm^{-2} with bare NF as reference (Fig. 3d). As expected, the P-NF-10 electrode at a potential of around 1.58 V (*vs.* RHE) maintained such industrial-grade current densities for 24 h without any degeneration in activity. In contrast, the activity of bare NF rapidly decreased under the same working environment. Notably, the C_{dl} of P-NF-10 measured after 24 h laboratory CP almost doubled, indicating the occurrence of surface reconstruction with increased active sites during the OER process, thereby accounting for its robust activity (Fig. 3c and Fig. S20). Moreover, when the CP experiment of P-NF-10 at 500 mA cm^{-2} was continued for a prolonged period, it still preserved its current density for over 120 h without any decay (Fig. S21). In addition to this, we determined 96% FE of the P-NF-10 electrode during the OER process, establishing its high catalytic activity (Fig. S22). Encouraged by this excellent electrocatalytic OER performance of P-NF-10, we further employed it as both anode and cathode to assemble an AWE, which showed a promising overall water-splitting activity under laboratory conditions (Fig. S23). Notably, when replacing the cathode as the highly efficient cathodic HER electrode (NiPt$_3$@NiS supported on NF) developed in our previous work [43], a distinctly better performance can be achieved by this upgraded electrolyzer, NiPt$_3$@NiS (-) // P-NF-10 (+), under laboratory conditions, which was also obviously superior to those of the AWEs integrated by commercial Pt/C deposited on NF (Pt/C/NF) cathode and P-NF-10 anode (Fig. S23). Furthermore, an even more satisfactory activity of NiPt$_3$@NiS (-) // P-NF-10 (+) can be obtained under the industrial scenario (Fig. 3e). The overall cell only required cell voltages of ~1.57 and ~1.72 V to afford the current density of 100 and 500 mA cm^{-2}, respectively, much better than that of presently employed industrial AWEs (over 1.8 V for 200–400 mA cm^{-2}) [17,44]. Such activity also outmatched most reported advanced assembled AWEs in the case of industrial environments, as demonstrated in Table S6. Another point

worth emphasizing here is that under such a harsh environment, the industry-level current density as high as 500 mA cm^{-2} can be maintained by our assembled AWE for over 107 h (Fig. 3 f). Although some progress has been made by a limited amount of reported TM-based AWEs for quasi-industrial application, they can hardly meet the industrial requirements such as high current densities, long-term and robust stability, as well as the increased concentration and temperature of electrolyte simultaneously [45–49]. Accordingly, in our case, the low-cost but excellent-performance P-incorporated NF prepared by the facile, scalable, and controllable CPE presents huge potential for practical water electrolysis.

As mentioned before, apart from 10 min, we also treated NF at different time intervals such as 1, 5, and 15 min (P-NF-1, P-NF-5, and P-NF-15). Their corresponding PXRD, SEM, and EDX result well elaborate that the CPE approach can precisely control the extent of P incorporation where a linearly increased amount of P with homogenous distribution on the activated NF surface was observed. Meanwhile, the surface morphology became progressively more porous and rough with the rise of CPE durations (Fig. 1 f and 2a−b, as well as Figs. S4−S5, S11 −S12, and S24 −S30, Table S1). On one hand, our CPE method presented the capability of rapid P atom incorporation (2% P was introduced into NF in merely 1 min). On the other hand, the P-content of P-NF-15 was found to be close to that of P-NF-10, suggesting that the P atoms nearly reached the incorporation saturation within the Ni host lattice after almost 10 mins of CPE treatment. To make this correlation more meaningful, we acquired and compared their LSV data, from which we found that even 1 min of CPE-induced P-incorporation can boost the OER performance of pristine NF, and the activity continuously increased up to an optimum CPE period of 10 mins (Fig. S31). Further prolonging the electrolysis to 15 min caused a slight performance deterioration, probably due to the agglomeration of surface-active regions after CPE overtreatment, which was also supported by the obtained EIS and C_{dl} results (Figs. S32−S33, and Table S5).

3.3. Insights into the active OER structure by ex-situ, in-situ and DFT analysis

In general, nearly all TM-based electrocatalysts undergo structural reconstructions during the anodic OER process, forming associated TM-based (oxy)hydroxides, which then serve as the real active species [6,16,25,50–53]. Therefore, to monitor this, a series of *in/ex-situ* post-OER (note that all the three samples investigated hereafter were those after 24 h CP at 500 mA cm^{-2}) characterizations were subsequently conducted to investigate the surface reconstruction and the (real) active surface structure during the OER influenced by the P-incorporation and different working environments. First of all, under laboratory conditions, the post-OER PXRD of both bare NF and P-NF-10 exhibit the same diffraction peaks as that of before OER, indicating that either the structures were stable or the *in-situ* evolved active species during OER were amorphous/low crystallinity. This observation is also consistent with the PXRD pattern of post-OER P-NF-10 under industrial conditions (Fig. S34). The corresponding HRTEM images of the surface species of P-NF-10 after both laboratory and industrial OER further confirm the amorphous/low-crystalline γ-Ni^{III}OOH (PDF#06–0075) evolved on the electrode surface during water oxidation (Fig. S35) [7]. On the other hand, the surface SEM images disclose that after laboratory OER CP, the surface morphology of P-NF-10 was more porous and rough with the layered-like feature in comparison to bare NF electrode, which still retained in a relatively flat morphology. It implies a deeper oxidative transformation of P-NF-10, leading to an enlarged specific surface area with increased active sites (Fig. 4a–b). Remarkably, their EDX mapping results of surface SEM and cross-sectional FIB-SEM further illustrate that such reconstructive oxidation was confined to the near-surface region of both CPE-treated and untreated NF electrodes. Simultaneously, both samples exhibited the obvious Fe doping, which originated from impurities in the KOH electrolyte during the OER process, facilitating the
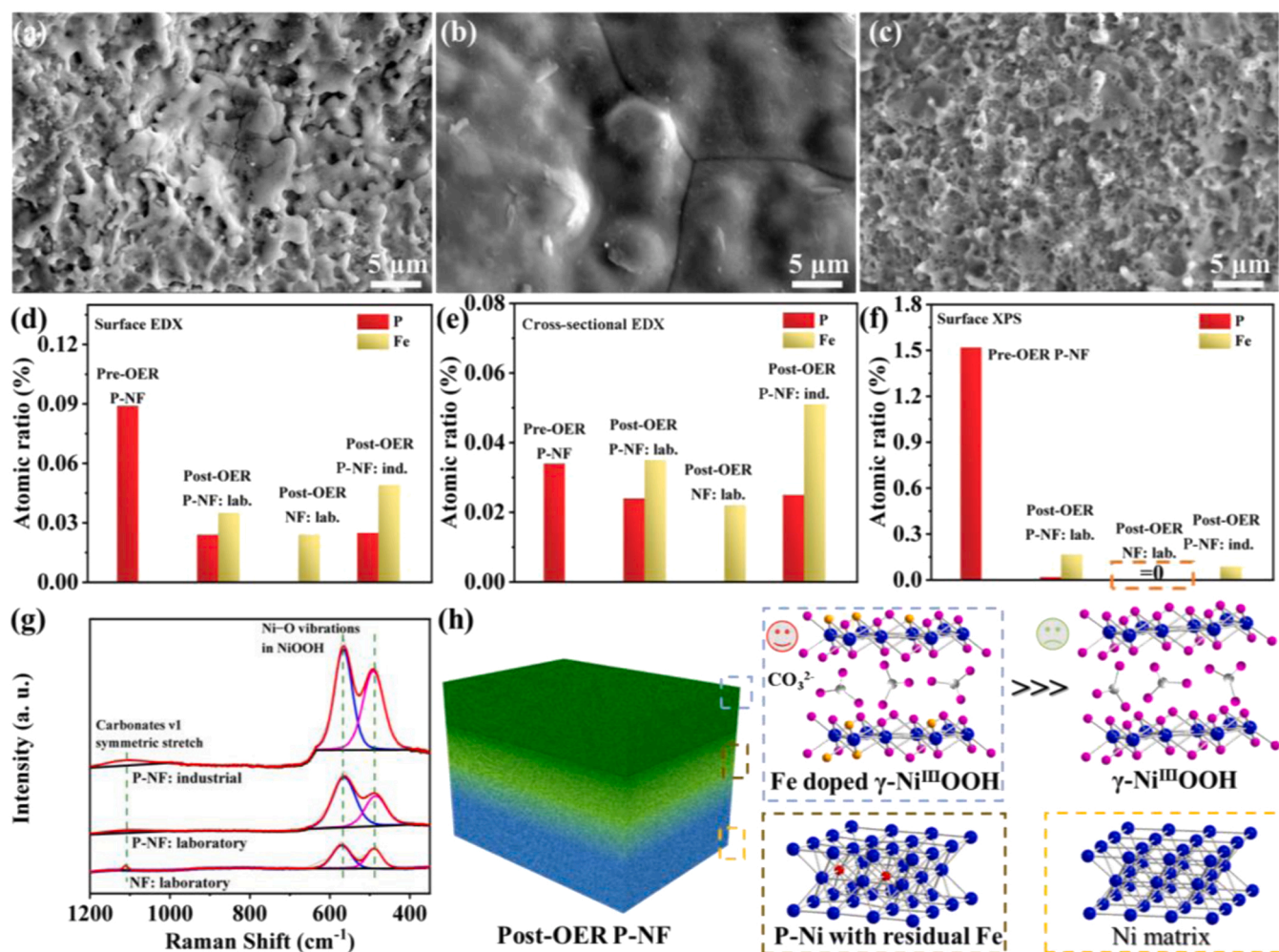
Fig. 4. The SEM images of electrodes after 24 h OER CP (at 500 mA cm^{-2}), including (a) P-NF-10 and (b) bare NF in laboratory conditions, as well as (c) P-NF-10 in industrial conditions; (d) Surface SEM-EDX, (e) cross-sectional FIB-SEM-EDX, and (f) XPS findings of the atomic ratio of P and Fe in pre-OER P-NF-10, post-OER P-NF-10 and bare NF at the laboratory level, as well as post-OER P-NF-10 at industrial level, respectively. Note that pre-OER P-NF-10 and post-OER bare NF themselves did not contain any Fe and P, respectively. Also, the Ni content in all characterizations was applied as the basis to calibrate the ratio of P and Fe, hence its atomic ratio was 1; (g) Quasi-*in-situ* Raman spectra of post-OER P-NF-10 and bare NF under laboratory conditions, as well as the P-NF-10 under industrial conditions; (h) The model of post-OER P-NF for the illustration of its structural reconstruction, in which blue, red, yellow, pink, and light grey spheres represent Ni, P, Fe, O and C atoms, respectively.

reconstruction most likely into Fe-containing (oxy)hydroxides (Figs. S36–S39) [25]. In analogy, the even more severe surface oxidation at both surface and near-surface areas can be found at the P-NF sample after OER CP under the harsher industrial environment. Also, EDX mapping confirms the impurity Fe incorporation (Fig. 4c and Figs. S40–S41). To further understand the content and distribution of all the elements, Fig. 4d–f summarizes the atomic ratio of elements for the above three films obtained *via* both surface EDX and cross-sectional FIB-EDX, as well as XPS investigations. Herein two points are worth being highlighted: i) Our samples were all fabricated, electrochemically measured, and post characterized exposing to air or (aqueous) electrolyte, thus their oxygen atomic ratio results were considered to be not sufficiently accurate (hence they were not used for the analyses), and only determination of other elements can clearly be deduced. ii) The XPS probing region is just confined at the maximum of 10 nm depth on the electrode surface because of the limited escape depth of the photoelectrons, while SEM-EDX is sensitive to various elements with a much larger detection thickness ranging from 0.2 to 8 μm [54,55]. Accordingly, three interesting phenomena can be found after the 24 h laboratory CP at 500 mA cm^{-2}: i) The incorporated P at the topmost surface of P-NF has leached out, leaving only the residual ones in the near-surface

area of P-NF; ii) The Fe dopants existed in both bare NF and P-NF, where more Fe had been incorporated into P-NF; iii) The presence of Fe can be detected from the surface to the near-surface area of the P-NF electrode, while the topmost layer of bare NF did not contain any Fe (more details in Figs. S36–S39, as well as Fig. 4d–f). More intriguingly, when comparing the post-OER P-NF under laboratory and industrial conditions, it can be observed that: i) They both lost most P during the OER process, while the remained P atoms were quantitatively close, which were accommodated at the near-surface area (the remaining P-Ni layer); ii) The harsher environment resulted in much higher Fe dopant concentration, but on the topmost surface the industrial-level post-OER P-NF revealed distinctly fewer Fe ions than the laboratory one (more details can be found in Figs. S36–S37 and S40–S41, as well as Fig. 4d–f). Note that the residual P content of P-NF-10 was independent of the OER duration, probably because the oxidative corrosion of P atoms at the near-surface region far from the outmost surface was insufficient (Fig. S42 and Table S7). In view of this, the outermost-sensitive XPS spectra of these abovementioned three samples were further analyzed, verifying that the reconstructed surface structure of bare NF in the laboratory state was pure Ni^{III}OOH. Conversely, with the leaching of surface P, Fe^{III}-doped Ni^{III}OOH evolved at the surface of P-NF during

both laboratory and industrial OER, and in the former case, more Fe can be immobilized in the surface transformed $Ni^{III}OOH$ structure (details in Fig. S43).

To shed more light on the *in-situ* surface reconstruction of the post-OER (CP at 500 mA cm^{-2} for 24 h) P-NF and NF under laboratory conditions, as well as the P-NF under industrial treatment, the quasi-*in-situ* Raman spectroscopy characterizations with high surface sensitivity were implemented by the freeze quenching (-196 °C) at the potentials when these three samples reached 500 mA cm^{-2}, respectively. As is displayed in Fig. 4g, for all of the probed three samples, the characteristic E_g bending and A_{1g} stretching vibration of Ni–O in $Ni^{III}OOH$ appeared at around 481 and 560 cm^{-1} in the Raman spectra, respectively. Particularly, the intensity ratio of these two bands (I_{Eg}/I_{A1g}) is widely accepted as a direct indicator of $Ni^{III}OOH$ structure with Fe doping, where: i) the lower the intensity ratio, the more Fe doping, and accordingly, ii) the more thorough transformation of Ni-based precatalysts into Fe doped $Ni^{III}OOH$ with better water oxidation activity (at least with less than 10% doped Fe) [26–29,56]. As expected, under the laboratory environment, the I_{Eg}/I_{A1g} of fitted Raman spectrum for post-OER P-NF (0.73) was distinctly lower than that of bare NF (0.88), while under industrial conditions the intensity ratio of fitted Raman spectrum for P-NF was also lower (0.84). This phenomenon was further confirmed by the above-analyzed OER performance, element content (especially for Fe dopants), and distribution impacted by P-incorporation and change in the working environment. Moreover, a Raman band at around 1063 cm^{-1} emerged for all three samples, representing $\nu1$ symmetric stretch of carbonate and validating that the *in-situ* formed $Ni^{III}OOH$ for these samples existed as the γ-phase. γ-$Ni^{III}OOH$ possesses a larger interlayer distance due to the intercalation of CO_3^{2-} ions from the dissolved carbonate in alkaline media [7,57]. Note that the industrial-related P-NF exhibited a much broader carbonate $\nu1$ band, which was probably induced by the larger concentration of KOH with more dissolved carbonates [58].

Thus, as elaborated in Fig. 4h, we could summarize that during the laboratory OER process, all the vital three components of P-NF, *i.e.*, Ni, Fe, and P atoms, underwent the dynamic structural reconstructions: i) on the P-NF surface, the surface metallic Ni atoms were oxidized into the layered γ-$Ni^{III}OOH$ structure whose interlayer space was intercalated with carbonates, serving as the real active matrix for OER; ii) impurity Fe atoms from the KOH electrolyte were concurrently doped into the *in-situ* formed γ-$Ni^{III}OOH$ structure, eventually leading to the emergence of one of the most efficient OER catalyst, Fe^{III}-doped $Ni^{III}OOH$, which was responsible for the excellent activity of the P-NF anode [28,29]; iii) almost all of the incorporated P atoms within the surface of P-NF anode leached out, while the residual P atoms were only presented at its near-surface region. Based on the obtained insights into the dynamic change of the P atoms, the role of P-incorporating on activating electrocatalytically inert NF can be generally summarized as follows: i) the introduction of P induced by *in-liquid* CPE enabled the treated NF to present high surface porosity and superhydrophilicity, as well as superior electrical conductivity, attaining the increment and utilization of active sites, and acceleration of transfer of electrons; more importantly, ii) at the initial state of the OER, the incorporated P atoms endowed the P-NF electrode with higher adsorption ability toward more impurity Fe atoms, thus presenting a higher Fe doping concentration; iii) with prolonging the OER, the incorporated P atoms at the outermost region of P-NF were dissolved, resulting in a more apparent porous surface morphology, which offered more opportunities for electrolyte penetration, enlarging the contacting areas between electrode and electrolyte, hence compensating Fe impurity redeposition/incorporation. It is worth pointing out that the surface dynamic dissolution of TM (especially doped Fe) easily transpires in the Ni-Fe system in alkaline media during the OER process [59,60], thus the maintenance of Fe doping can substantially facilitate the superior OER activity and stability of P-NF [28, 29]. On the other hand, in the case of bare NF, fewer Fe were doped during OER, this is probably because of the relatively flat and smooth surface morphology of NF that cannot stabilize the Fe dopants within the bare NF-derived γ-$Ni^{III}OOH$. The dissolution of surface doped Fe of bare NF was probably more kinetically favorable than the redeposition/incorporation induced by the lack of effective compensation (flat surface morphology preserved during OER), and consequently, no surface Fe dopants can be found in the bare NF-derived γ-$Ni^{III}OOH$. For P-NF in the industrial OER, similar to that under laboratory conditions, the Fe^{III}-doped γ-$Ni^{III}OOH$ structure was also reconstructed on the electrode surface. The only difference is that fewer incorporated Fe atoms were present on the topmost surface (more surface Fe leaching might be induced by the harsher working environment compared with that of ambient OER [61]), which was probably the key factor contributing to the slight decrease in activity. Additionally, we discovered that the OER activity of P-NF-10 was enhanced with the increment of the initial concentration of iron ions in the fresh 1 M KOH electrolyte, which can promote more Fe doping into the electrode during OER and be independent of the P leaching degree. Therefore, the *in-situ* reconstructed γ-$Ni^{III}OOH$ with higher Fe^{III}-doping evolved on the electrode surface (Figs. S44–S46 and Table S7).

3.4. Selective electrooxidation of aldehydes

The bifunctional catalytic oxidation ability of P-NF-10 was further explored by selective electrooxidation of aldehydes, which can generate higher economically valuable products at the anode compared to O_2 obtained *via* OER [12–14]. Recently, a series of efficient non-noble metal-based electrocatalysts have emerged as a possible replacement for standard OER catalysts with selective anodic oxidation of various alcohols or 5-hydroxymethylfurfural [62–65]. However, their ability to electrooxidize aldehydes, specifically furan-2-carboxaldehyde (furfural) and acetaldehyde (CH_3CHO), has been rather unexplored. Furan-2-carboxaldehyde oxidation produces furan-2-carboxylic acid (2-furoic acid, Scheme S1) with significant economic values in the food industry, biomedical research, optical technology, as well as nylon production [66–68]. In addition, the acetic acid (CH_3COOH) derived from the selective CH_3CHO oxidation (Scheme S2) is frequently utilized as a high-boiling polar solvent in standard organic synthesis [12]. Therefore, developing highly efficient but low-cost non-noble electrocatalysts for the selective oxidation of aldehydes is of tremendous economic and practical significance. Given the high anodic OER performance, we used P-NF-10 to selectively oxidize the furan-2-carboxaldehyde and CH_3CHO. Also, the untreated bare NF was considered for comparison.

First, LSVs were measured in a three-electrode system using P-NF-10 or bare NF as the working electrode in 1 M KOH with and without 0.1 M furfural. As shown in Fig. 5a, starting from 1.38 V (*vs.* RHE) the current densities of both P-NF-10 and bare NF, with the addition of 0.1 M furan-2-carboxaldehyde, distinctly increased compared to the pure KOH electrolyte. To further endorse the higher activity of the CPE-treated films for aldehyde oxidation, we performed chronoamperometry (CA) at a constant potential of 1.49 V *vs.* RHE with 0.1 M furan-2-carboxaldehyde using P-NF or bare NF as the anode. As shown in Fig. 5b, P-NF-10 displayed a significantly higher organic substrate oxidation current density than that of bare NF. To probe the conversion of furan-2-carboxaldehyde oxidation products catalyzed by P-NF-10 and bare NF, the reaction solutions before and after CA were characterized through ^1H NMR spectroscopy (Fig. 5c). Remarkably, after 65 min of CA with the passed charge of 192.96 C (a theoretical charge for the complete oxidation of furfural to 2-furoic acid), P-NF-10 catalyst achieved as high as 94% for both product conversion and FE, while bare NF (58.62 C of charge passed after 65 min) showed only 42% conversion with the FE of 82% (Fig. 5d). The ^1H NMR conversion of furfural to 2-furoic acid was quantified by using dimethylsulfone as an internal standard (Figs. S47–S48). Furthermore, under identical testing conditions, the electrocatalytic oxidation of acetaldehyde (CH_3CHO) into acetic acid (CH_3COOH) using P-NF-10 as an anode demonstrated a high conversion
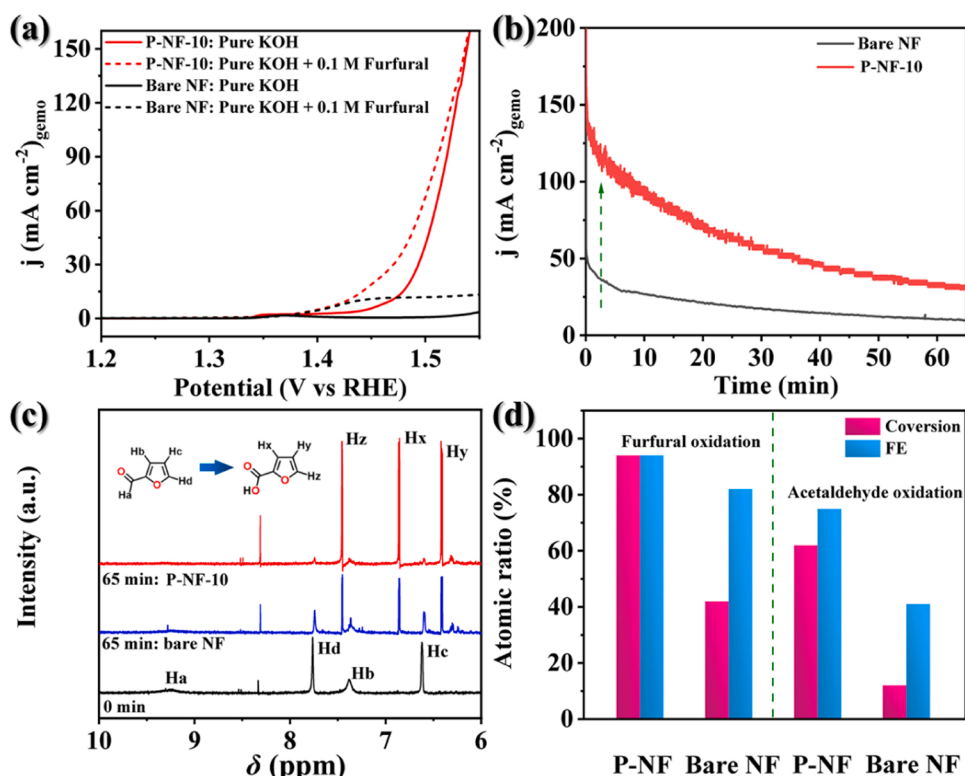
Fig. 5. (a) The LSV curves of P-NF-10 and bare NF in 1 M KOH electrolyte with and without 0.1 M furan-2-carboxaldehyde; (b) The CA curves of P-NF-10 and bare NF in 1 M KOH electrolyte with 0.1 M furan-2-carboxaldehyde at a constant potential of 1.49 V (*vs.* RHE); (c) Pre- and post-CA ^{1}H NMR spectrum of P-NF-10 and bare NF towards the reaction solutions under bulk electrolysis; (d) Conversion and FE of P-NF-10 and bare NF to electrooxidize furan-2-carboxaldehyde and acetaldehyde, respectively.

of 62% with the FE of 75%, significantly higher than the results obtained with bare NF (12% acetic acid conversion with 41% FE) (Fig. 5d and Figs. S49–S50). All the above results indicate that the P-incorporation through the CPE treatment activated NF with exceptional electro-oxidation capability of aldehydes. According to the previous reports of Ni-based electrocatalysts for alcohol and aldehyde oxidation, one widely accepted reaction mechanism is that the redox-active Ni atoms tend to *in-situ* reconstruct into surface Ni^{III}OOH intermediates with electrophilic oxygen groups, which then attack the nucleophilic reagents, thus facilitating the process of electrooxidation [69–71]. Based on this mechanism, the most effective approaches to elevating the electrooxidation ability are mainly based on: i) increased number of accessible redox active Ni sites on the catalyst surface, ii) acceleration of the mass diffusion and transport, iii) enhancement of electric conductivity of the whole Ni-based catalysts, and iv) improvement of the intrinsic activity of catalytic Ni species [72–78].

In this regard, the P-NF-10 developed in our case was directly compared with the bare NF which behaved poorly for selective aldehyde oxidation. The advantages of P-incorporation to enhance the electro-oxidation capability can be explained with the following aspects: i) the introduction of P atoms induced by CPE treatment facilitated the NF surface with distinctly high porosity and roughness, which can enormously increase the specific surface area and accordingly expose more surface redox-active Ni sites (Fig. 2a–b, Figs. S11–S12 and S19a–b); ii) at the same time, the wettability of the treated NF was tuned into super-hydrophilicity, which effectively endowed the electrolyte (organic substrates) access to the electrode surface, therefore contributing to the increase in mass diffusion and transport and the surface reaction kinetics (insets of Fig. 2a–b); iii) the substitution of P atoms to Ni in the nickel lattice can severely modify its electronic structure, hence accelerating the inherent electron transfer ability of the treated NF, as elaborated by the total density of state (TDOS) changes (Fig. 2d and Fig. S15). Similarly, the XPS comparison between P-NF-10 and bare NF (Fig. S10) uncovers that Ni atoms donated a partial electron to the incorporated neighboring P atoms, which has been reported to be conducive to

improving inherent activity of the catalytic Ni sites for aldehyde oxidation [78]. As a result, all the above factors synergistically promoted the P-NF-10 anode to show a remarkably improved aldehyde oxidation ability than that of commercial bare NF.

4. Conclusion

In summary, aiming at answering the abovementioned research questions (i–iv), we have successfully employed the controllable, facile, and ultrafast CPE method to induce P atoms into bare NF. The as-prepared P-NF exhibited enhanced surface porosity and wettability and improved electric conductivity. Strikingly, the presence of P in NF significantly improved the adsorption ability of Fe doping atoms. Consequently, in 1 M KOH containing Fe impurities at room temperature, the optimized P-NF-10 electrode behaved with excellent OER activity, achieving a current density of 500 mA cm^{-2} at an overpotential of only ~350 mV, outmatching bare NF and commercial noble metal-based IrO$_2$ on NF. Notably, the latter higher current density was maintained well over 120 h, suggesting exceptional durability of P-NF under operating conditions. Most importantly, P-NF-10 was utilized as an anode in a quasi-industrial alkaline water electrolyzer (6 M KOH and 60 °C), delivering as high as 500 mA cm^{-2} current density at ~1.72 V cell voltage with the long-term stability of over 107 h. The question (v) was addressed using a combination of *ex/in-situ* characterization techniques, illustrating that even at higher surface porosity induced by intensive oxidation and surface P-leaching, P-NF can maintain the equilibrium of the dissolution and redeposition/incorporation of the doped Fe impurities during OER, thereby forming Fe^{III}-doped surface reconstructed γ-Ni^{III}OOH, while the surface of bare NF just evolved into pure γ-Ni^{III}OOH. Finally, to address question (vi), P-NF was investigated for the rarely explored but industrially important organic substrates furan-2-carboxaldehyde and acetaldehyde, yielding high catalytic oxidation efficiency and selectivity. Thus, our novel CPE approach for the rapid and facile activation of the substrate will be a great leap forward for the economic electrode fabrication of large-scale hydrogen

generation and value-added industrial products.

CRediT authorship contribution statement

Hongyuan Yang: Investigation, Validation, Data curation, Writing – original draft. **Pramod V. Menezes:** Investigation, Validation, Data curation. **Guoliang Dai:** Data curation, Software. **Gonela Vijaykumar:** Investigation. **Ziliang Chen:** Investigation. **Mohammad Al-Shakran**: Investigation. **Timo Jacob:** Resources, Writing – review & editing. **Matthias Driess:** Resources, Writing – review & editing, Funding acquisition. **Prashanth W. Menezes:** Conceptualization, Methodology, Supervision, Project administration, Writing – review & editing, Funding acquisition.

Declaration of Competing Interest

The authors declare that they have no known competing financial interests or personal relationships that could have appeared to influence the work reported in this paper.

Data Availability

Data will be made available on request.

Acknowledgements

Appendix A. Supporting information

Supplementary data associated with this article can be found in the online version at doi:10.1016/j.apcatb.2022.122249.

References

[1] Z.Z.W. Seh, J. Kibsgaard, C.F. Dickens, I. Chorkendorff, J.K. Nørskov, T. F. Jaramillo, Combining theory and experiment in electrocatalysis: Insights into materials design, Science 335 (2017) 146, https://doi.org/10.1126/science.aad4998.
[2] H. Xu, H. Jia, B. Fei, Y. Ha, H. Li, Y. Guo, M. Liu, R. Wu, Charge transfer engineering via multiple heteroatom doping in dual carbon-coupled cobalt phosphides for highly efficient overall water splitting, Appl. Catal. B: Environ. 268 (2020) 118404, https://doi.org/10.1016/j.apcatb.2019.118404.
[3] Z. Chen, H. Yang, Z. Kang, M. Driess, P.W. Menezes, The pivotal role of s-, p-, and f-block metals in water electrolysis: Status quo and perspectives, Adv. Mater. 34 (2022), 2108432, https://doi.org/10.1002/adma.202108432.
[4] H. Yang, J. Liu, Z. Chen, R. Wang, B. Fei, H. Liu, Y. Guo, R. Wu, Unconventional bi-vacancies activating inert Prussian blue analogues nanocubes for efficient hydrogen evolution, Chem. Eng. J. 420 (2021) 127671, https://doi.org/10.1016/j.cej.2020.127671.
[5] S. Anantharaj, S. Noda, V.R. Jothi, S. Yi, M. Driess, P.W. Menezes, Strategies and perspectives to catch the missing pieces in energy-efficient hydrogen evolution reaction in alkaline media, Angew. Chem. Int. Ed. 60 (2021) 18981, https://doi.org/10.1002/anie.202015738.
[6] H. Yang, G. Dai, Z. Chen, J. Wu, H. Huang, Y. Liu, M. Shao, Z. Kang, Pseudo-periodically coupling Ni-O lattice with Ce-O lattice in ultrathin heterononawire arrays for efficient water oxidation, Small 17 (2021) 2101727, https://doi.org/10.1002/smll.202101727.
[7] P.W. Menezes, S. Yao, R. Beltrán-Suito, J.N. Hausmann, P.V. Menezes, M. Driess, Facile access to an active γ-NiOOH electrocatalyst for durable water oxidation derived from an intermetallic nickel germanide precursor, Angew. Chem. Int. Ed. 60 (2021) 4640, https://doi.org/10.1002/anie.202014331.
[8] J. Zhou, L. Yu, Q. Zhou, C. Huang, Y. Zhang, B. Yu, Y. Yu, Ultrafast fabrication of porous transition metal foams for efficient electrocatalytic water splitting, Appl. Catal. B: Environ. 288 (2021), 120002, https://doi.org/10.1016/j.apcatb.2021.120002.
[9] Q. Hu, Z. Wang, X. Huang, Y. Qin, H. Yang, X. Ren, Q. Zhang, J. Liu, M. Shao, C. He, Integrating well-controlled core-shell structures into "superaerophobic" electrodes for water oxidation at large current densities, Appl. Catal. B: Environ. 286 (2021), 119920, https://doi.org/10.1016/j.apcatb.2021.119920.
[10] P. Zhang, X. Sheng, X. Chen, Z. Fang, J. Jiang, M. Wang, F. Li, L. Fan, Y. Ren, B. Zhang, B.J.J. Timmer, M.S.G. Ahlquist, L. Sun, Paired electrocatalytic oxygenation and hydrogenation of organic substrates with water as the oxygen and hydrogen source, Angew. Chem. Int. Ed. 58 (2019) 9155, https://doi.org/10.1002/anie.201903936.
[11] B. Zhu, C. Chen, L. Huai, Z. Zhou, L. Wang, J. Zhang, 2,5-Bis(hydroxymethyl)furan: a new alternative to HMF for simultaneously electrocatalytic production of FDCA and H2 over CoOOH/Ni electrodes, Appl. Catal. B Environ. 297 (2021), 120396, https://doi.org/10.1016/j.apcatb.2021.120396.
[12] P.W. Menezes, C. Walter, B. Chakraborty, J.N. Hausmann, I. Zaharieva, A. Frick, E. von Hauff, H. Dau, M. Driess, Combination of highly efficient electrocatalytic water oxidation with selective oxygenation of organic substrates using manganese borophosphates, Adv. Mater. 33 (2021), 2004098, https://doi.org/10.1002/adma.202004098.
[13] B. Chakraborty, R. Beltrán-Suito, J.N. Hausmann, S. Garai, M. Driess, P. W. Menezes, Enabling iron-based highly effective electrochemical water-splitting and selective oxygenation of organic substrates through in situ surface modification of intermetallic iron stannide precatalyst, Adv. Energy Mater. 10 (2020), 2001377, https://doi.org/10.1002/aenm.202001377.
[14] J.N. Hausmann, R. Beltrán-Suito, S. Mebs, V. Hlukhyy, T.F. Fässler, H. Dau, M. Driess, P.W. Menezes, Evolving highly active oxidic iron(III) phase from corrosion of intermetallic iron silicide to master efficient electrocatalytic water oxidation and selective oxygenation of 5-hydroxymethylfurfural, Adv. Mater. 33 (2021), 2008823, https://doi.org/10.1002/adma.202008823.
[15] B. Zhong, P. Kuang, L. Wang, J. Yu, Hierarchical porous nickel supported NiFeOxHy nanosheets for efficient and robust oxygen evolution electrocatalyst under industrial condition, Appl. Catal. B Environ. Volume 299 (2021), 120668, https://doi.org/10.1016/j.apcatb.2021.120668.
[16] H. Yang, M. Driess, P.W. Menezes, Self-supported electrocatalysts for practical water electrolysis, Adv. Energy Mater. 11 (2021), 2102074, https://doi.org/10.1002/aenm.202102074.
[17] L. Zhuang, Y. Jia, H. Liu, Z. Li, M. Li, L. Zhang, X. Wang, D. Yang, Z. Zhu, X. Yao, Sulfur-modified oxygen vacancies in iron–cobalt oxide nanosheets: Enabling extremely high activity of the oxygen evolution reaction to achieve the industrial water splitting benchmark, Angew. Chem. Int. Ed. 59 (2020) 14664, https://doi.org/10.1002/anie.202006546.
[18] H. Yang, Z. Chen, W. Hao, H. Xu, Y. Guo, R. Wu, Catalyzing overall water splitting at an ultralow cell voltage of 1.42 V via coupled Co-doped NiO nanosheets with carbon, Appl. Catal. B Environ. 252 (2019) 214, https://doi.org/10.1016/j.apcatb.2019.04.021.
[19] H. Yang, Z. Chen, P. Guo, B. Fei, R. Wu, B-doping-induced amorphization of LDH for large-current-density hydrogen evolution reaction, Appl. Catal. B Environ. 261 (2020), 118240, https://doi.org/10.1016/j.apcatb.2019.118240.
[20] H. Yang, P. Guo, R. Wang, Z. Chen, H. Xu, H. Pan, D. Sun, F. Fang, R. Wu, Sequential phase conversion-induced phosphides heterononarod arrays for superior hydrogen evolution performance to Pt in wide pH media, Adv. Mater. (2022), 2107548, https://doi.org/10.1002/adma.202107548.
[21] L. Yu, L. Wu, B. McElhenny, S. Song, D. Luo, F. Zhang, Y. Yu, S. Chen, Z. Ren, Ultrafast room-temperature synthesis of porous S-doped Ni/Fe (oxy)hydroxide electrodes for oxygen evolution catalysis in seawater splitting, Energy Environ. Sci. 13 (2020) 3439, https://doi.org/10.1039/D0EE00921K.
[22] Y. Pan, Y. Yao, C. Liang, Y. Zhang, J. Chen, Q. Li, Plasma mediated preparation of NiFeNx nanoparticles anchored on nickel foam for efficient oxygen evolution in alkaline solution, Mater. Lett. 302 (2021), 130371, https://doi.org/10.1016/j.matlet.2021.130371.
[23] W. Zhu, T. Zhang, Y. Zhang, Z. Yue, Y. Li, R. Wang, Y. Jia, X. Sun, J. Wang, A practical-oriented NiFe-based water-oxidation catalyst enabled by ambient redox and hydrolysis co-precipitation strategy, Appl. Catal. B: Environ. 244 (2019) 844, https://doi.org/10.1016/j.apcatb.2018.12.021.
[24] Z. Wang, S. Wang, L. Ma, Y. Guo, J. Sun, N. Zhang, R. Jiang, Water-induced formation of Ni2P–Ni12P5 interfaces with superior electrocatalytic activity toward hydrogen evolution reaction, Small 17 (2021), 2006770, https://doi.org/10.1002/smll.202006770.
[25] Y.J. Son, K. Kawashima, B.R. Wygant, C.H. Lam, J.N. Burrow, H. Celio, A. Dolocan, J.G. Ekerdt, C.B. Mullins, Anodized nickel foam for oxygen evolution reaction in Fe-free and unpurified alkaline electrolytes at high current densities, ACS Nano 15 (2021) 3468, https://doi.org/10.1021/acsnano.0c10788.
[26] K. Zhu, X. Zhu, W. Yang, Application of in situ techniques for the characterization of NiFe-based oxygen evolution reaction (OER) electrocatalysts, Angew. Chem. Int. Ed. 58 (2019) 1252, https://doi.org/10.1002/anie.201802923.
[27] M.W. Louie, A.T. Bell, An investigation of thin-film Ni–Fe oxide catalysts for the electrochemical evolution of oxygen, J. Am. Chem. Soc. 135 (2013) 12329, https://doi.org/10.1021/ja405315s.
[28] S. Klaus, Y. Cai, M.W. Louie, L. Trotochaud, A.T. Bell, Effects of Fe electrolyte impurities on Ni(OH)2/NiOOH structure and oxygen evolution activity, J. Phys. Chem. C. 119 (2015) 7243, https://doi.org/10.1021/acs.jpcc.5b00105.
[29] L. Trotochaud, S.L. Young, J.K. Ranney, S.W. Boettcher, Nickel–iron oxyhydroxide oxygen-evolution electrocatalysts: the role of intentional and incidental iron

incorporation, J. Am. Chem. Soc. 136 (2014) 6744, https://doi.org/10.1021/ja502379c.

[30] C. Sun, J. Zeng, H. Lei, W. Yang, Q. Zhang, Direct electrodeposition of phosphorus-doped nickel superstructures from choline chloride–ethylene glycol deep eutectic solvent for enhanced hydrogen evolution catalysis, ACS Sustain. Chem. Eng. 7 (2019) 1529, https://doi.org/10.1021/acssuschemeng.8b05302.

[31] V.H. Hoa, D.T. Tran, D.C. Nguyen, D.H. Kim, N.H. Kim, J.H. Lee, Molybdenum and phosphorous dual doping in cobalt monolayer interfacial assembled cobalt nanowires for efficient overall water splitting, Adv. Funct. Mater. 30 (2020), 2002533, https://doi.org/10.1002/adfm.202002533.

[32] H. Jin, X. Liu, S. Chen, A. Vasileff, L. Li, Y. Jiao, L. Song, Y. Zheng, S. Qiao, Heteroatom-doped transition metal electrocatalysts for hydrogen evolution reaction, *A*CS Energy Lett. 4 (2019) 805, https://doi.org/10.1021/acsenergylett.9b00348.

[33] B. Zhang, F. Yang, X. Lium, N. Wu, S. Che, Y. Li, Phosphorus doped nickel-molybdenum aerogel for efficient overall water splitting, Appl. Catal. B: Environ. 298 (2021), 120494, https://doi.org/10.1016/j.apcatb.2021.120494.

[34] Y. Shi, B. Zhang, Recent advances in transition metal phosphide nanomaterials: synthesis and applications in hydrogen evolution reaction, Chem. Soc. Rev. 45 (2016) 1529, https://doi.org/10.1039/C5CS00434A.

[35] J. Duan, S. Chen, C.A. Ortíz-Ledón, M. Jaroniec, S. Qiao, Phosphorus vacancies that boost electrocatalytic hydrogen evolution by two orders of magnitude, Angew. Chem. Int. Ed. 59 (2020) 8181, https://doi.org/10.1002/anie.201914967.

[36] Q. Dong, M. Li, M. Sun, F. Si, Q. Gao, X. Cai, Y. Xu, T. Yuan, S. Zhang, F. Peng, Y. Fang, S. Yan, Phase-controllable growth Ni$_x$P$_y$ modified CdS@Ni$_3$S$_2$ electrodes for efficient electrocatalytic and enhanced photoassisted electrocatalytic overall water splitting, Small Methods 5 (2021), 2100878, https://doi.org/10.1002/smtd.202100878.

[37] M. Aliofkhazraei, A.S. Rouhaghdam, P. Gupta, Nano-fabrication by cathodic plasma electrolysis, Crit. Rev. Solid State Mater. Sci. 36 (2011) 174, https://doi.org/10.1080/10408436.2011.593269.

[38] J. Wu, W. Xue, B. Wang, X. Jin, J. Du, Y. Li, Characterization of carburized layer on T8 steel fabricated by cathodic plasma electrolysis, Surf. Coat. Technol. 245 (2014) 9, https://doi.org/10.1016/j.surfcoat.2014.02.024.

[39] E.I. Meletis, X. Nie, F. Wang, J. Jiang, Electrolytic plasma processing for cleaning and metal-coating of steel surfaces, Surf. Coat. Technol. 150 (2002) 246, https://doi.org/10.1016/S0257-8972(01)01521-3.

[40] P. Gupta, G. Tenhundfeld, E.O. Daigle, D. Ryabkov, Electrolytic plasma technology: science and engineering—an overview, Surf. Coat. Technol. 201 (2007) 8746, https://doi.org/10.1016/j.surfcoat.2006.11.023.

[41] S. Yao, V. Forstner, P.W. Menezes, C. Panda, S. Mebs, E.M. Zolnhofer, M. E. Miehlich, T. Szilvási, N.A. Kuma, M. Haumann, K. Meyer, H. Grützmacher, M. Driess, From an Fe$_2$P$_3$ complex to FeP nanoparticles as efficient electrocatalysts for water-splitting, Chem. Sci. 9 (2018) 8590, https://doi.org/10.1039/C8SC03407A.

[42] J.N. Hausmann, B. Traynor, R.J. Myers, M. Driess, P.W. Menezes, The pH of aqueous NaOH/KOH solutions: a critical and non-trivial parameter for electrocatalysis, ACS Energy Lett. 6 (10) (2021) 3567, https://doi.org/10.1021/acsenergylett.1c01693.

[43] C. Panda, P.W. Menezes, S. Yao, J. Schmidt, C. Walter, J.N. Hausmann, M. Driess, Boosting electrocatalytic hydrogen evolution activity with a NiPt$_3$@NiS heteronanostructure evolved from a molecular nickel–platinum precursor, J. Am. Chem. Soc. 141 (2019) 13306–13310, https://doi.org/10.1021/jacs.9b06530.

[44] M. Carmo, D.L. Fritz, J. Mergel, D. Stolten, A comprehensive review on PEM water electrolysis, Int. J. Hydrog. Energy 38 (2013) 4901, https://doi.org/10.1016/j.ijhydene.2013.01.151.

[45] Y. Tan, Q. Li, Q. Che, X. Chen, X. Xu, Y. Chen, Improving activity of Ni$_3$P/Mn hybrid film via electrochemical tuning for water splitting under simulated industrial environment, Electrochim. Acta 324 (2019) 134897, https://doi.org/10.1016/j.electacta.2019.134897.

[46] H. Zhou, F. Yu, Q. Zhu, J. Sun, F. Qin, L. Yu, J. Bao, Y. Yu, S. Chen, Z. Ren, Water splitting by electrolysis at high current densities under 1.6 volts, Energy Environ. Sci. 11 (2018) 2858, https://doi.org/10.1039/C8EE00927A.

[47] Y. Wu, H. He, Electrodeposited nickel–iron–carbon–molybdenum film as efficient bifunctional electrocatalyst for overall water splitting in alkaline solution, Int. J. Hydrog. Energy 44 (2019) 1336, https://doi.org/10.1016/j.ijhydene.2018.11.168.

[48] J. Lian, Y. Wu, H. Zhang, S. Gu, Z. Zeng, X. Ye, One-step synthesis of amorphous Ni–Fe–P alloy as bifunctional electrocatalyst for overall water splitting in alkaline medium, Int. J. Hydrog. Energy 43 (2018) 12929, https://doi.org/10.1016/j.ijhydene.2018.05.107.

[49] B. Ren, D. Li, Q. Jin, H. Cui, C. Wang, In-situ tailoring cobalt nickel molybdenum oxide components for overall water-splitting at high current densities, ChemElectroChem 6 (2019) 413, https://doi.org/10.1002/celc.201801386.

[50] C. Walter, P.W. Menezes, M. Driess, Perspective on intermetallics towards efficient electrocatalytic water-splitting, Chem. Sci. 12 (2021) 8603, https://doi.org/10.1039/D1SC01901E.

[51] J.N. Hausmann, R.A. Khalaniya, C. Das, I. Remy-Speckmann, S. Berendts, A. V. Shevelkov, M. Driess, P.W. Menezes, Intermetallic Fe$_6$Ge$_5$ formation and decay of a core–shell structure during the oxygen evolution reaction, Chem. Commun. 57 (2021) 2184, https://doi.org/10.1039/D0CC08035G.

[52] J.N. Hausmann, S. Mebs, K. Laun, I. Zebger, H. Dau, P.W. Menezes, M. Driess, Understanding the formation of bulk- and surface-active layered (oxy)hydroxides for water oxidation starting from a cobalt selenite precursor, Energy Environ. Sci. 13 (2020) 3607, https://doi.org/10.1039/D0EE01912G.

[53] H. Yang, J.N. Hausmann, V. Hlukhyy, T. Braun, K. Laun, I. Zebger, M. Driess, P. W. Menezes, An intermetallic CaFe$_6$Ge$_6$ approach to unprecedented Ca−Fe−O

electrocatalyst for efficient alkaline oxygen evolution reaction, ChemCatChem 14 (2022), e202200293, https://doi.org/10.1002/cctc.202200293.

[54] A.M. Venezia, X-ray photoelectron spectroscopy (XPS) for catalysts characterization, Catal. Today 77 (2003) 359, https://doi.org/10.1016/S0920-5861(02)00380-2.

[55] M.J. Walzak, R. Davidson, M. Biesinger, The use of XPS, FTIR, SEM/EDX, contact angle, and AFM in the characterization of coatings, J. Mater. Eng. Perform. 7 (1998) 317, https://doi.org/10.1361/105994998770347747.

[56] S. Anantharaj, S. Kundu, S. Noda, "The Fe Effect": A review unveiling the critical roles of Fe in enhancing OER activity of Ni and Co based catalysts, Nano Energy 80 (2021), 105514, https://doi.org/10.1016/j.nanoen.2020.105514.

[57] B.M. Hunter, W. Hieringer, J.R. Winkler, H.B. Gray, A.M. Muller, Effect of interlayer anions on [NiFe]-LDH nanosheet water oxidation activity, Energy Environ. Sci. 9 (2016) 1734, https://doi.org/10.1039/C6EE00377J.

[58] M. Wang, R. Qian, M. Bao, C. Gu, P. Zhu, Raman, FT-IR and XRD study of bovine bone mineral and carbonated apatites with different carbonate levels, Mater. Lett. 210 (2018) 203, https://doi.org/10.1016/j.matlet.2017.09.023.

[59] C. Kuai, Z. Xu, C. Xi, A. Hu, Z. Yang, Y. Zhang, C. Sun, L. Li, D. Sokaras, C. Dong, S. Qiao, X. Du, F. Lin, Phase segregation reversibility in mixed-metal hydroxide water oxidation catalysts, Nat. Catal. 3 (2020) 743, https://doi.org/10.1038/s41929-020-0496-z.

[60] C. Kuai, C. Xi, A. Hu, Y. Zhang, Z. Xu, D. Nordlund, C. Sun, C.A. Cadigan, R. M. Richards, L. Li, C. Dong, X. Du, F. Lin, Revealing the dynamics and roles of iron incorporation in nickel hydroxide water oxidation catalysts, J. Am. Chem. Soc. 143 (2021) 18519, https://doi.org/10.1021/jacs.1c07975.

[61] C. Feng, F. Wang, Z. Liu, M. Nakabayashi, Y. Xiao, Q. Zeng, J. Fu, Q. Wu, C. Cui, Y. Han, N. Shibata, K. Domen, I.D. Sharp, Y. Li, A self-healing catalyst for electrocatalytic and photoelectrochemical oxygen evolution in highly alkaline conditions, Nat. Commun. 12 (2021) 5980, https://doi.org/10.1038/s41467-021-26281-0.

[62] B. Mondal, N. Karjule, C. Singh, R. Shimoni, M. Volokh, I. Hod, M. Shalom, Unraveling the mechanisms of electrocatalytic oxygenation and dehydrogenation of organic molecules to value-added chemicals over a Ni–Fe oxide catalyst, Adv. Energy Mater. 11 (2021), 2101858, https://doi.org/10.1002/aenm.202101858.

[63] N. Wang, X. Li, M. Hu, W. Wei, S. Zhou, X. Wu, Q. Zhu, Ordered macroporous superstructure of bifunctional cobalt phosphide with heteroatomic modification for paired hydrogen production and polyethylene terephthalate plastic recycling, Appl. Catal. B Environ. 316 (2022), 121667, https://doi.org/10.1002/adma.202104791.

[64] Y. Lu, C. Dong, Y. Huang, Y. Zou, Z. Liu, Y. Liu, Y. Li, N. He, J. Shi, S. Wang, Identifying the geometric site dependence of spinel oxides for the electrooxidation of 5-hydroxymethylfurfural, Angew. Chem. Int. Ed. 59 (2020) 19215, https://doi.org/10.1002/anie.202007767.

[65] J. Zheng, X. Chen, X. Zhong, S. Li, T. Liu, G. Zhuang, X. Li, S. Deng, D. Mei, J. Wang, Hierarchical porous NC@CuCo nitride nanosheet networks: Highly efficient bifunctional electrocatalyst for overall water splitting and selective electrooxidation of benzyl alcohol, Adv. Funct. Mater. 27 (2017), 1704169, https://doi.org/10.1002/adfm.201704169.

[66] P. Varelis, B. Hucker, Thermal decarboxylation of 2-furoic acid and its implication for the formation of furan in foods, Food Chem. 126 (2011) 1512, https://doi.org/10.1016/j.foodchem.2010.12.017.

[67] B. Uma, K.S. Murugesan, S. Krishnan, S.J. Das, B.M. Boaz, Optical and dielectric studies on organic nonlinear optical 2-furoic acid single crystals, Optik 124 (2013) 2754, https://doi.org/10.1016/j.ijleo.2012.08.075.

[68] R. Mariscal, P. Maireles-Torres, M. Ojeda, I. Sadaba, M.L. Granados, Furfural: a renewable and versatile platform molecule for the synthesis of chemicals and fuels, Energy Environ. Sci. 9 (2016) 1144, https://doi.org/10.1039/C5EE02666K.

[69] J.N. Hausmann, P.V. Menezes, G. Vijaykumar, K. Laun, T. Diemant, I. Zebger, T. Jacob, M. Driess, P.W. Menezes, In-liquid plasma modified nickel foam: NiOOH/NiFeOOH active site multiplication for electrocatalytic alcohol, aldehyde, and water oxidation, Adv. Energy Mater. 12 (2022), 2202098, https://doi.org/10.1002/aenm.202202098.

[70] M.M. Khalaf, H.M.A. El-Lateef, A.O. Alnajjar, I.M.A. Mohamed, A facile chemical synthesis of Cu$_x$Ni$_{(1−x)}$Fe$_2$O$_4$ nanoparticles as a nonprecious ferrite material for electrocatalytic oxidation of acetaldehyde, Sci. Rep. 10 (2020) 2761, https://doi.org/10.1038/s41598-020-59655-3.

[71] W. Gou, Y. Chen, Y. Zhong, Q. Xue, J. Li, Y. Ma, Phytate-coordinated nickel foam with enriched NiOOH intermediates for 5-hydroxymethylfurfural electrooxidation, Chem. Commun. 58 (2022) 7626–7629, https://doi.org/10.1039/D2CC02182J.

[72] Z. Zhao, T. Guo, X. Luo, X. Qin, L. Zheng, L. Yu, Z. Lv, D. Ma, H. Zheng, Bimetallic sites and coordination effects: electronic structure engineering of NiCo-based sulfide for 5-hydroxymethylfurfural electrooxidation, Catal. Sci. Technol. 12 (2022) 3817–3825, https://doi.org/10.1039/D2CY00281G.

[73] X. Wu, X. Wang, Z. Wu, Design principle of electrocatalysts for the electrooxidation of organics, Chem 8 (2022) 2594–2629, https://doi.org/10.1016/j.chempr.2022.07.010.

[74] J. Woo, B.C. Moon, U. Lee, H. Oh, K.H. Chae, Y. Jun, B.K. Min, D.K. Lee, Collaborative electrochemical oxidation of the alcohol and aldehyde groups of 5–Hydroxymethylfurfural by NiOOH and Cu(OH)2 for superior 2,5-furandicar-boxylic acid production, ACS Catal. 12 (2022) 4078–4091, https://doi.org/10.1021/acscatal.1c05341.

[75] J. Zhang, X. Song, L. Kang, J. Zhu, L. Liu, Q. Zhang, D.J.L. Brett, P.R. Shearing, L. Mai, I.P. Parkin, G. He, Stabilizing efficient structures of superwetting electrocatalysts for enhanced urea oxidation reactions, Chem. Catal. 2 (2022) 1–17, https://doi.org/10.1016/j.checat.2022.09.023.

[76] T. Eisa, H.O. Mohamed, Y. Choi, S. Park, R. Ali, M.A. Abdelkareem, S. Oh, K. Chae, Nickel nanorods over nickel foam as standalone anode for direct alkaline methanol and ethanol fuel cell, Int. J. Hydrog. Energy 45 (2020) 5948–5959, https://doi.org/10.1016/j.ijhydene.2019.08.071.

[77] M. Xing, D. Zhang, D. Liu, C. Song, D. Wang, Surface engineering of carbon-coated cobalt-doped nickel phosphides bifunctional electrocatalyst for boosting 5-hydroxymethylfurfural oxidation coupled with hydrogen evolution, J. Colloid Interface Sci. 629 (2023) 451–460, https://doi.org/10.1016/j.jcis.2022.09.091.

[78] X. Bai, W. He, X. Lu, Y. Fu, W. Qi, Electrochemical oxidation of 5-hydroxymethylfurfural on ternary metal–organic framework nanoarrays: enhancement from electronic structure modulation, J. Mater. Chem. A 9 (2021) 14270–14275, https://doi.org/10.1039/D1TA02464G.